

Is Betelgeuse really rotating? Synthetic ALMA observations of large-scale convection in 3D simulations of Red Supergiants

JING-ZE MA (马竞泽) ¹ ANDREA CHIAVASSA ^{2,1} SELMA E. DE MINK ^{1,3} RUGGERO VALLI ¹
STEPHEN JUSTHAM ^{1,4,5} AND BERND FREYTAG ⁶

¹Max Planck Institute for Astrophysics, Karl-Schwarzschild-Str. 1, 85748 Garching, Germany

²Université Côte d'Azur, Observatoire de la Côte d'Azur, CNRS, Lagrange, CS 34229, Nice, France

³Anton Pannekoek Institute for Astronomy and GRAPPA, University of Amsterdam, NL-1090 GE Amsterdam, The Netherlands

⁴School of Astronomy & Space Science, University of the Chinese Academy of Sciences, Beijing 100012, China

⁵National Astronomical Observatories, Chinese Academy of Sciences, Beijing 100012, China

⁶Theoretical Astrophysics, Department of Physics and Astronomy, Uppsala University, Box 516, SE-751 20 Uppsala, Sweden

ABSTRACT

The evolved stages of massive stars are poorly understood, but invaluable constraints can be derived from spatially resolved observations of nearby red supergiants, such as Betelgeuse. ALMA observations of Betelgeuse showing a dipolar velocity field have been interpreted as evidence for a rotation rate of $v \sin i \sim 5 \text{ km s}^{-1}$. This is two orders of magnitude larger than predicted by single-star evolution, leading to the suggestion that Betelgeuse is a binary merger product. We propose instead that the velocity field could be due to large-scale convective motions. The resulting surface velocity maps can sometimes be mistaken for rotation, especially when the turbulent motions are only partially resolved, as is the case for the current ALMA beam. We support this claim with 3D CO5BOLD simulations of *non-rotating* red supergiants post-processed to predict synthetic ALMA images and SiO spectra to compare with observed radial velocity maps. Our simulations show a $\sim 50\%$ chance to be interpreted as evidence for a rotation rate as high as claimed for Betelgeuse. We conclude that we need at least another ALMA observation to firmly establish whether Betelgeuse is indeed rapidly rotating. Such observations would also provide insight into the role of angular momentum and binary interaction in the late evolutionary stages. The data will further probe the structure and complex physical processes in the atmospheres of red supergiants, which are immediate progenitors of supernovae and are believed to be essential in the formation of gravitational wave sources.

1. INTRODUCTION

Cool evolved stars are not expected to be rotating fast, at least not at their surfaces. As the stars evolve, their envelopes expand by one to two orders of magnitude. The outer layers thus slow down as a result of angular momentum conservation and may be further reduced by, e.g. mass loss due to stellar winds (e.g. Maeder & Meynet 2000; Smith 2014), possibly inward convective transport of angular momentum (e.g. Brun & Toomre 2002; Brun & Palacios 2009), and magnetic braking (Mestel 1968). The theory of single star evolution therefore predicts slow surface rotation rates, less than about 1 km s^{-1} for stars at the tip of the red giant branch (e.g. Privitera et al. 2016a), and less than about 0.1 km s^{-1} for red supergiants (RSGs; Wheeler et al. 2017; Chatzopoulos et al. 2020), which are the cool giant descendants of massive stars.

Despite theoretical expectations, cool stars with rotation rates exceeding these predictions have been observed across the Hertzsprung-Russell diagram. These include several hundred red giants, about 1% of the total population of red giants (e.g. Patton et al. 2023, and references therein), and a few asymptotic giant branch (AGB) stars (Barnbaum et al. 1995; Vlemmings et al. 2018; Brunner et al. 2019; Nhung et al. 2021, 2023). For RSGs, so far only one has been claimed to rotate rapidly: α Orionis, better known as Betelgeuse (Uitenbroek et al. 1998; Harper & Brown 2006; Kervella et al. 2018), which recently has drawn wide attention after the sudden Great Dimming (Guinan et al. 2019) and subsequent re-brightening (Guinan et al. 2020).

Betelgeuse, being one of the closest RSGs to Earth, is one of the few stars that can be spatially resolved and has therefore been a target of interferometric studies for over a century (Michelson & Pease 1921). Recently, the Atacama Large Millimeter/submillimeter Array (ALMA) provided unprecedented maps of the molecular envelope (Kervella et al. 2018, hereafter K18; right-

hand panels of our Figure 2). The surface radial velocity map shows a remarkably clear dipolar structure: half of the visible hemisphere of the star shows a blue shift and the other half shows a red shift of several km s^{-1} .

A natural explanation of such a dipolar velocity field is stellar rotation, as noted by K18. They inferred a projected equatorial velocity of $v \sin i = 5.47 \pm 0.25 \text{ km s}^{-1}$. They compared the results with earlier measurements using the Hubble Space Telescope (HST) probing the chromosphere (Uitenbroek et al. 1998; Harper & Brown 2006) and argued that both the ALMA and HST data are consistent with the interpretation that Betelgeuse is fast-rotating. The fast rotation rate inferred for Betelgeuse is surprising in light of the predictions of single-star models, as illustrated in Figure 1 and Appendix A for details.

Binary star evolution has been proposed as an explanation for Betelgeuse’s high rotation rate, in particular the merger with a lower mass companion (Wheeler et al. 2017; Chatzopoulos et al. 2020; Sullivan et al. 2020; Shiber et al. 2023). This may seem like an exotic explanation, but massive stars often interact with close companions (Sana et al. 2012). As a consequence, stellar mergers are expected to be common (de Mink et al. 2014; Kochanek et al. 2014). Zapartas et al. (2019) estimated that as many as one-third of RSGs experience a stellar merger before they reach core collapse. Rui & Fuller (2021) identified two dozen red giants that are possible merger products, based on their asteroseismological signatures. For red giants, the engulfment of planets has also been proposed as an explanation for their rapid rotation (Carlberg et al. 2012; Privitera et al. 2016b; Gaulme et al. 2020; Lau et al. 2022).

Establishing whether Betelgeuse is indeed rotating, is of vital importance to better understand its evolutionary history, the possible role of binary interaction, and the physics of the evolved stages of massive stars in general (see Wheeler & Chatzopoulos 2023, for a review). Unfortunately, accurate and reliable measurements of rotation rates for red (super)giants are challenging.

The first complicating factor concerns the high velocities expected for convective flows at the photosphere. These may be as high as 20 km s^{-1} , as shown in different 3D simulations (Kravchenko et al. 2019; Antoni & Quataert 2022; Goldberg et al. 2022) as well as spectroscopic (Lobel & Dupree 2000; Josselin & Plez 2007) and optical interferometric observations (Ohnaka et al. 2009, 2011, 2013, 2017). This is two orders of magnitude larger than the predicted rotational velocities and four times larger than the rotational velocity inferred for Betelgeuse by K18. How the turbulent velocity field affects the measurement of the rotation rate is not yet well understood.

A second complication concerns the large sizes expected for the convective cells at the surface, which may span a significant fraction of the radius (Schwarzschild 1975). Only a few of them will be present at the surface

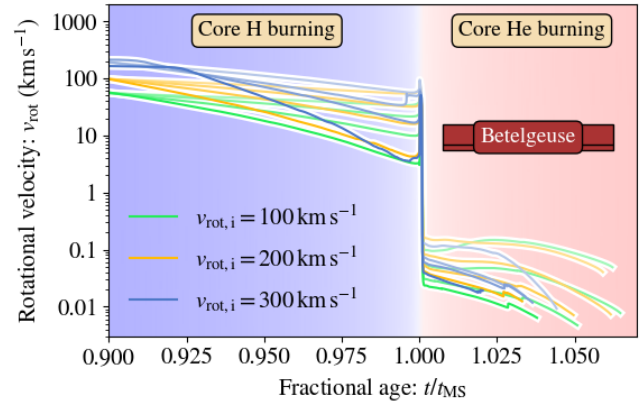


Figure 1. The equatorial rotational velocity inferred for Betelgeuse (K18) is 2–3 orders of magnitude higher than single-star models predict. To illustrate this point, we show MESA predictions for the rotational velocities of massive stars ($\sim 10 - 20 M_{\odot}$) with typical initial rotation rates as a function of their fractional age, i.e. time divided by their main sequence lifetime. The steep drop in rotation rates marks the rapid expansion as stars transition from the core H-burning phase (blue background) to the core He-burning RSGs (red background). See Appendix A for details.

at any given time, as also suggested by spectropolarimetric (Ariste et al. 2018, 2022) and optical interferometric observations (e.g. Haubois et al. 2009; Norris et al. 2021). If, by chance, one very large cell or a group of cells move toward the observer while others move away, this can result in a dipolar velocity field even for a *non-rotating* star.

The central question motivating our current study is: “Can a *non-rotating* red (super)giant be mistaken to be a rapid rotator?” For our study, we use existing 3D radiation hydrodynamic simulations of RSGs with properties similar to Betelgeuse. We develop a new post-processing package to solve the radiative transfer equations and make direct predictions for ALMA observables that we compare with observations of Betelgeuse. We quantify how fast a *non-rotating* star can appear to be rotating and how likely it is to obtain spurious measurements of high rotation. We conclude that, to firmly establish whether Betelgeuse is rotating rapidly, additional epochs of ALMA observations are needed, preferably with higher spatial resolution.

2. METHOD

2.1. 3D simulations of RSG envelope with CO5BOLD

To assess whether a *non-rotating* RSG can show a dipolar radial velocity map in the ALMA band, we need global 3D RSG models that simulate the multi-scale convection of the full star. So far this is only possible with the CO5BOLD models (Freytag et al. 2012), since other 3D RSG models do not simulate the whole 4π sphere (Goldberg et al. 2022). We use existing 3D

radiation-hydrodynamic simulations of RSG convective envelopes from [Ahmad et al. \(2023\)](#), computed with the CO5BOLD code. The CO5BOLD RSG simulations have been extensively used to interpret spectro-photometric, interferometric, and astrometric observations, especially in the context of Betelgeuse (e.g. [Chiavassa et al. 2009, 2010; Montargès et al. 2014, 2016; Kravchenko et al. 2021](#)). The code numerically integrates the nonlinear compressible hydrodynamic equations, coupled with a short-characteristics scheme for radiation transport ([Freytag et al. 2012](#)). The global simulations that we use in this work adopt the ‘star-in-a-box’ setup by simulating the outer part of the convective envelope with mass M_{env} on an equidistant Cartesian grid. The interior is replaced by an artificial central region providing a luminosity source with a drag force to damp the velocity. A gravitational potential is imposed, set by the central mass M_{pot} . For the gravity experienced by the simulation, the stellar mass is M_{pot} because the self-gravity of the envelope is neglected. However, for actual stars, the total stellar mass would be $M_{\text{pot}} + M_{\text{env}}$. For detailed descriptions of the general setup, see [Chiavassa et al. \(2011a\)](#), [Freytag et al. \(2012\)](#) and [Chiavassa et al. \(2024, submitted\)](#).

We use the simulation of a *non-rotating* star with large surface convective cells, given by the surface gravity $\log_{10} g = -0.419$ in cgs units and effective temperature $T_{\text{eff}} = 3366$ K, close to the observed values for Betelgeuse (see Table 2 in Appendix D). An alternative simulation, with smaller surface convective cell sizes but which fits better with the mass and luminosity inferred for Betelgeuse, is presented and discussed in Appendix D.

2.2. Synthetic ALMA images

We post-process the 3D simulations to create synthetic observations for ALMA. Here we describe the main assumptions. Details and tests for each step are provided in Appendix C. The post-processing package, animations and data behind the figures are publicly available at Zenodo: doi: [10.5281/zenodo.10199936](https://doi.org/10.5281/zenodo.10199936).

To directly compare with the SiO line spectra observed by ALMA, we need to calculate the intensity from SiO emission and absorption. For the chemical abundances of the relevant species (SiO molecules, the electrons and atomic H), we use the equilibrium-chemistry code FASTCHEM2¹ ([Stock et al. 2018, 2022](#)). FASTCHEM2 has been widely adopted and tested against observations of exoplanetary atmosphere, in particular for ultra-hot jupiters where the day-side conditions are similar to cool stars (e.g. [Kitzmann et al. 2018, 2023](#)). For AGB atmospheres which share similar convective properties with RSGs, chemical equilibrium was shown to be a reasonable approximation ([Agúndez](#)

et al. 2020). Here, we present the first application of FASTCHEM2 to stellar atmospheres.

To synthesize the intensity map, we numerically integrate the radiative transfer equation on a Cartesian grid. We take into account the continuum free-free opacity and Doppler-shifted ²⁸SiO lines (vibrational level $\nu = 2$, rotational transition $J = 8 - 7$ as observed by ALMA). Detailed equations and opacity sources can be found in Appendix C.2.

We scale the simulation such that the radio photospheric radius approximately matches ALMA observations in K18 (For the associated limitations, see Appendix C.4). We interpolate the intensities onto a 101^2 pixel grid, such that both the pixel number and the angular coverage are identical to ALMA observations. We then convolve the intensity map with the ALMA beam (FWHM of 18 mas). We use the convolved continuum intensity map to calculate the radius of the radio photosphere $R_{\text{star}} = \sqrt{\int I(r, \theta) r dr d\theta / (\pi I_{\text{star}})}$ where the integral is performed over the 2D image (Section 3.3.1 in K18). Here, I is the continuum intensity as a function of the polar coordinate (r, θ) on the 2D image, measured in the spectral window centered at 343.38 GHz as done in ALMA observations. Its value at the photocenter is denoted as I_{star} .

2.3. Analysis to the radial velocity map

To compare our simulations with the observed radial velocity maps, we follow the analysis in K18. We use the continuum-subtracted intensities to identify the line in each pixel, fit a Gaussian profile to the line using least squares fitting, and obtain the radial velocity shift from the central value of the Gaussian. The apparent systematic velocity v_{sys} is obtained from the radial velocity shift of the integrated line (over the region up to 30 mas from the center for the absorption line and 30 – 50 mas for the emission line as in Section 3.3.2 in K18).

We measure the apparent $v \sin i$ by fitting the projected radial velocity map of a rigidly-rotating sphere to the v_{sys} -subtracted radial velocity map within R_{star} (Section 3.5 in K18, however, see a more detailed discussion in Appendix C.3 for the choice of the radius adopted). Since both the observing time and the orientation of the star with respect to the observer are arbitrary, we repeat this procedure for six faces of the Cartesian box and every snapshot of the simulations. Throughout the main text, we use the radial velocity maps derived from emission lines in accordance with the actual observations of K18.

3. RESULTS

3.1. Selected mock observations compared to actual ALMA observations

In Figure 2, we show a selected example of a synthetic ALMA image from our *non-rotating* RSG simulation, and compare it with the ALMA observations of Betel-

¹ <https://github.com/exoclimate/FastChem>

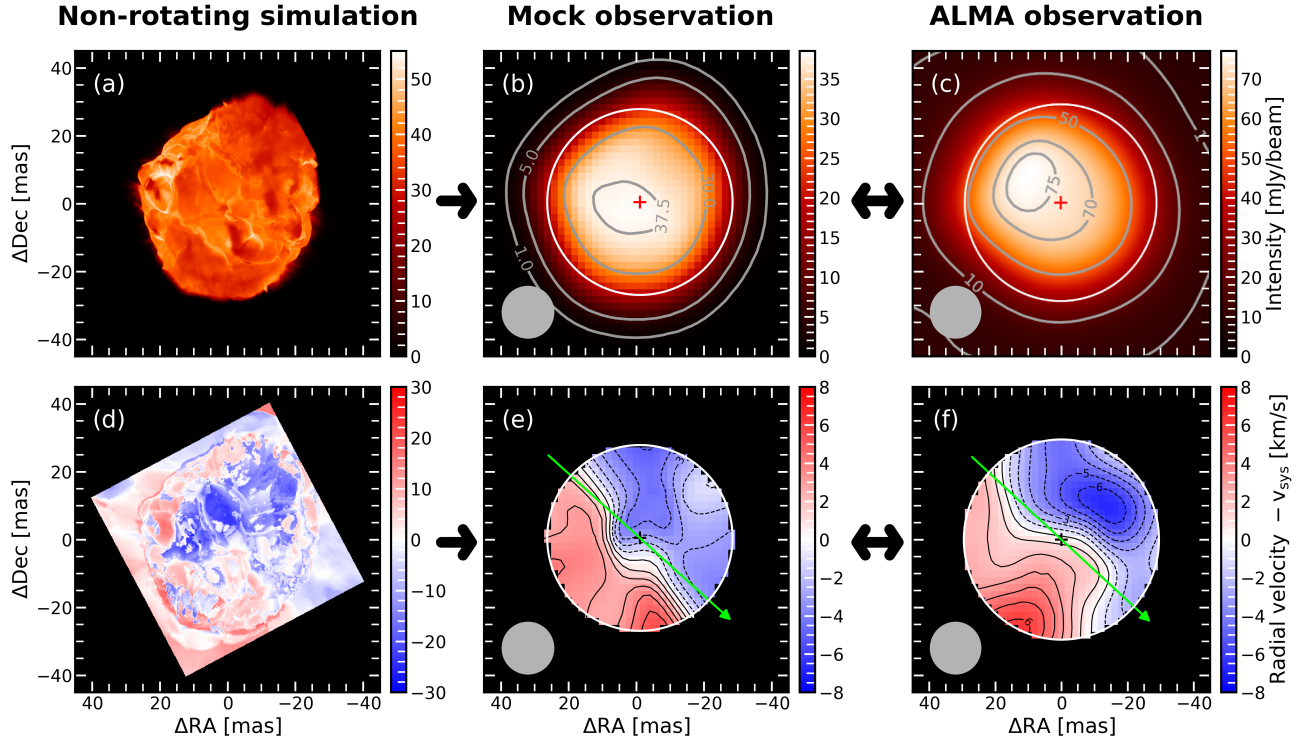


Figure 2. A direct comparison of a *non-rotating* RSG simulation with ALMA observations of Betelgeuse. For this figure, we have chosen an illustrative example of a simulation snapshot in time and orientation, where the *non-rotating* simulation can be easily mistaken as rotation. The left panels show the unconvolved simulation image (a & d). The middle panels show the convolved synthetic image (b & e). The right panels show the actual ALMA observations (c & f) from K18. The ALMA beam size is indicated by the gray circles. The top row demonstrates the continuum intensity maps. The measured radii R_{star} of the radio photosphere are indicated in white circles. The bottom row shows the radial velocity maps measured from the Doppler shift of SiO lines. The green arrows indicate the rotational axes from the fit. Images from the simulation are rotated such that the rotational axis aligns with the observed axis. Credit for the right two panels: Kervella et al., A&A, 609, A67, 2018, reproduced with permission © ESO. This figure is available as an animation in the HTML version of the paper as well as on Zenodo: doi: [10.5281/zenodo.10199936](https://doi.org/10.5281/zenodo.10199936) for our 5-year-long mock observations.

geuse in K18. The left-hand panels (a & d) show the original simulation. The middle panels (b & e) show our synthetic observations after convolution with the ALMA beam. The right-hand panels (c & f) show the actual ALMA observations (K18). In the top row, we show the simulated and observed continuum intensity maps. In the bottom row, we show the radial velocity maps measured from the Doppler shifts of the lines.

The unconvolved intensity map at these wavelengths probes the atmospheric layers of the star which are highly asymmetric (Figure 1a). The convective motions of $\pm 30 \text{ km s}^{-1}$ can be seen in the radial velocity map of the original simulations (Figure 1d). Both the cell size and the peak convective velocity are consistent with analytical estimates (Appendix B) and other 3D simulations of RSGs (Kravchenko et al. 2019; Antoni & Quataert 2022; Goldberg et al. 2022).

The ALMA beam used in the settings by K18 is about 30% of the diameter of the radio photosphere. This means that any sharp features on the surface will be smoothed out. The effect of this can be seen when

comparing the left and middle panels in Figure 1. For the intensity map, a single hot spot emerges (Figure 1b), similar to what is observed by ALMA (Figure 1c). Such a feature has also been observed in other images of Betelgeuse in the UV (Gilliland & Dupree 1996), optical (Young et al. 2000; Haubois et al. 2009; Montargès et al. 2016), and radio (O’Gorman et al. 2017). For the radial velocity map, positive and negative radial velocity shifts partially cancel each other after convolution with the beam size. This blurs the original radial velocity map with convective motions up to 30 km s^{-1} (Figure 1d) into a map with radial velocity variations up to 8 km s^{-1} (Figure 1e) consistent with the ALMA observations. We conclude that the synthetic images of the intensity map and radial velocity qualitatively match the main features of the observations. In particular, both synthetic and observed radial velocity maps (Figure 1e and f) show a dipolar velocity field, with one hemisphere approaching the observer and the other receding.

K18 interpreted the dipolar velocity field as a sign of rotation. Fitting for this, assuming rigid rotation, they

inferred a $v \sin i$ of $5.47 \pm 0.10 \text{ km s}^{-1}$, and a residual velocity dispersion of 1.44 km s^{-1} . Following the same procedure for our synthetic image, we obtain very similar values, see Table 1. The resulting χ_{red}^2 is larger than observed, but comparable within an order of magnitude. As shown in Figure 10 in Appendix D, if we have underestimated the overall smearing effect of the observational pipeline, the χ_{red}^2 may be vastly decreased.

Table 1. Comparison of fitting parameters of a *non-rotating* RSG simulation with ALMA observations of Betelgeuse. The radial velocity maps being fitted are shown in Figure 2. A rigidly-rotating model is used to fit the radial velocity maps to obtain the perceived projected rotation rate $v \sin i$ and fitting parameters (standard deviation of the residual σ_{res} and reduced χ_{red}^2). All the parameters are obtained using the method described in Section 2.3.

Inferred parameters	$v \sin i$ [km s^{-1}]	σ_{res} [km s^{-1}]	χ_{red}^2
Mock observation (this work, non-rotating)	5.51 ± 0.21	1.68	94.6
ALMA observation (K18)	5.47 ± 0.10	1.44	20.7

Note, however, that our simulation is based on a *non-rotating* star. The dipolar velocity field shown in the synthetic image is not the result of rotation, but the alignment of the group motions of the surface convective cells. The example shown here illustrates how turbulent motions in the atmosphere of a *non-rotating* RSG can, at certain times, mimic the effect of rotation. This raises the question of how confident we are that Betelgeuse is rotating and to what extent the expected large-scale convection affects the rotation measurement.

3.2. Probability of inferring rotation from the radial velocity map of a non-rotating RSG

In the previous section, we showed an example of how a *non-rotating* simulation can appear to be rotating as a result of under-resolved convective motions. We had chosen a particular snapshot in time that illustrates this point well. In this section, we discuss how often such situations occur. We present the distribution of inferred $v \sin i$ in our mock observations for the simulated RSG. To obtain the probability distribution of inferred $v \sin i$ in a single-epoch observation, we compile 480 inferred $v \sin i$ calculated for 6 faces and 80 snapshots (uniformly taken across the 5-year time span of the relaxed simulation) and plot the distribution in Figure 3.

Figure 3 shows that the apparent $v \sin i$ distribution inferred for our *non-rotating* models peaks at $\sim 5 \text{ km s}^{-1}$. The observed values for Betelgeuse (grey vertical lines) fall into the 50% probability interval around the peak. These simulations thus show that it is rather

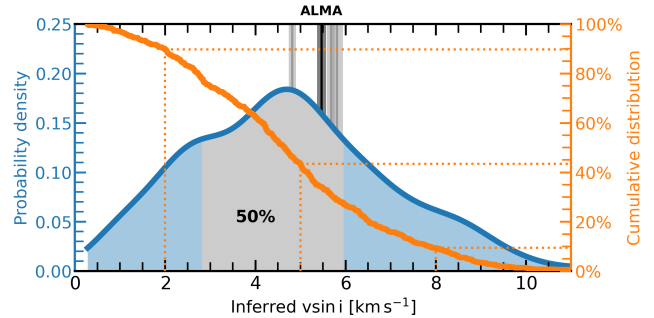


Figure 3. Probability distribution of apparent $v \sin i$ resulting from turbulent motions above the surface of a *non-rotating* stellar model. The grey vertical lines indicate the observed values based on SiO and CO lines (K18), with their uncertainties indicated by the widths and the SiO line we have modeled shown darker. The blue curve illustrates the kernel-smoothed probability density function of the inferred $v \sin i$. The 50% probability interval around the peak is shaded in grey. The orange curve shows the cumulative distribution function.

common that turbulent motions give rise to apparent $v \sin i$ similar to what is observed for Betelgeuse. We further show that for a *non-rotating* RSG to be interpreted as rotating faster than $\sim 5 \text{ km s}^{-1}$, the probability still remains as high as $\sim 40\%$. These numbers depend on the simulation adopted, and the parameters assumed for Betelgeuse, which are not well-constrained (Dolan et al. 2016; Joyce et al. 2020). Nevertheless, from the distribution we expect that $\sim 90\%$ single-epoch observations would show signs of rotation faster than $\sim 2 \text{ km s}^{-1}$. By visual inspection, the majority of those with inferred $v \sin i \lesssim 2 \text{ km s}^{-1}$ do not show an obvious dipolar structure that could be mistaken for rotation.

4. DISCUSSION

In Section 3, we argued that convective motions may be responsible for the dipolar velocity field observed for Betelgeuse, as an alternative to the explanation of rapid rotation. The quantitative results we presented are subject to uncertainties, due to the choices for the model parameters and limitations of simulations. We discuss this further in Appendix C.4 & D. Despite the uncertainties, we can use these results to formulate conceptual physical pictures that can be tested with future observations. In Figure 4 we illustrate three scenarios that, in principle, can explain the dipolar velocity map observed for the molecular shell around Betelgeuse.

- I. **Rapid rotation:** This hypothesis, proposed by K18, states that Betelgeuse is rapidly rotating and drags the surrounding molecular shell along.
- II. **Large convective cells and stochastic effects:** In this hypothesis, only very few convective cells cover the surface leading to stochastic effects (e.g.

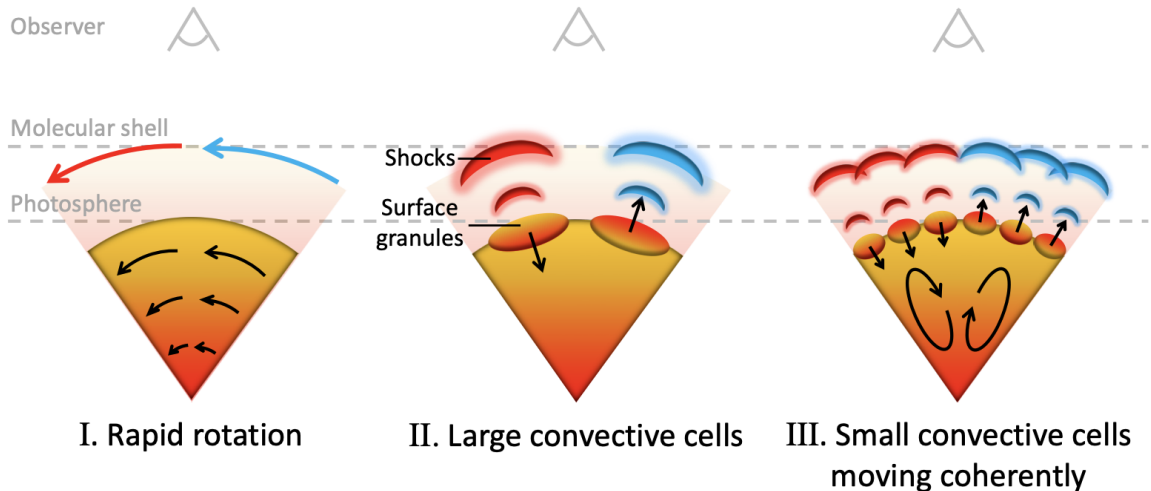


Figure 4. Three interpretations of Betelgeuse’s dipolar radial velocity map observed by ALMA. The physical pictures and their observational consequences are explained in Section 4.

Schwarzschild 1975). At certain times, only two large cells may dominate the dynamics of the hemisphere. If one cell moves outward and one inward, and the motions are transported to the molecular shell via waves or shocks, this would result in a dipolar velocity field.

III. Smaller convective cells moving coherently: A dipolar velocity field may also arise when the convective cells are smaller but move semi-coherently in groups. This physical picture most closely describes what we see in our simulations, where coherent motion is the result of deeper convective motions that operate over a length scale comparable to the stellar radius. Other mechanisms, e.g. non-radial oscillations (Lobel & Dupree 2001), may also be able to drive such coherent motions.

Note that, in principle, the rotational velocity field and the turbulent motions can co-exist in the molecular layer. The three hypotheses we list here emphasize which of the components *dominate* the velocity field.

4.1. Current observational constraints

All three hypotheses we consider can reproduce the dipolar radial velocity map. Here we mention further observational constraints that argue in favor or against the scenarios depicted in Fig. 4.

Support for the rotation hypothesis (I) has been claimed based on HST data probing the chromosphere of Betelgeuse (Uitenbroek et al. 1998; Harper & Brown 2006). They found an upward trend in the radial velocity while scanning over the surface from northwest to southeast, and interpreted this as being the result of rotation. The magnitude and direction of the inferred rotation are consistent with the data taken by K18 almost 20 years later.

This interpretation of the HST data is not without controversy. The radial velocities vary between observations taken a few months apart (see Fig. 6 in Harper & Brown 2006). Other HST data analyzed by Lobel & Dupree (2001) instead shows evidence for a reversal of velocities and Jadlovský et al. (2023) found no sign of rotation. These findings are more consistent with hypotheses (II) and (III), although it is unclear what the effect is of the great dimming event in the last study.

Evidence for the presence of (large) convective cells can be found in the asymmetries in the surface intensity map observed by ALMA, but also in earlier data probing the UV, optical, and radio, as discussed in Sect. 3. Specifically, the infrared images taken with VLTI/MATISSE, which probe the bottom part of the molecular layer with a spatial resolution of 4 mas (Drevon et al. 2024), show multiple resolved structures. Other nearby RSGs such as Antares, V602 Car and AZ Cyg show similar evidence (Ohnaka et al. 2017; Clement et al. 2020; Norris et al. 2021).

A further indication for turbulent motions at the molecular shell is the integrated line broadening observed by ALMA. The observed broadening of FWHM 24 km s^{-1} (Section 3.3.2 in K18) is significantly larger than what can be explained by the claimed rotation rate of 5.5 km s^{-1} . This line width is consistent with what we predict in our simulations, about 18 km s^{-1} on average. There is thus evidence for additional broadening, likely originating from convective motions, consistent with hypotheses (II) and (III).

4.2. Future observations to test the hypotheses

The hypotheses we propose have clear predictions that can be tested with future observations. In particular, additional epochs and higher spatial resolution are desired to resolve the variable radial velocity map.

Additional epochs will allow us to probe changes in the velocity field over time. In the case of rapid rotation (hypothesis I), we expect that the radial velocity map will not change significantly. Both the magnitude of the rotation and alignment of the spin axis should be close to values obtained in 2015 by K18. Instead, if the velocity field is dominated by turbulent motions, we expect the surface to readjust. Convective cells at the surface (hypothesis II) are expected to change on timescales of a few months (see e.g. Montargès et al. 2018; Norris et al. 2021, for RSG CE Tauri and AZ Cyg). Convective motions in the deep layers (hypothesis III) may take years, see Appendix B for an order of magnitude estimate. We expect the surface velocity field to significantly change on these timescales. The field may still be dipolar, but likely with a different orientation, or not display a dipolar feature.

Based on the 3D simulations we presented in this work, we estimate that in a single-epoch observation, there is a 50% chance that a *non-rotating* RSG appears to rotate as fast as observed (Figure 3). Assuming that there is no preferred direction and allowing for 20-degree uncertainty in the rotational axis, we expect a $20/360 \times 50\% \simeq 2\%$ chance that a second epoch for a non-rotating RSG will give a similar radial velocity map as observed in 2015 by coincidence. Therefore, this idealized example indicates that one additional single-epoch observation would be sufficient to test the rotation hypothesis at a confidence level equivalent to two sigma.

Observations of the radial velocity map at increased spatial resolution will also help distinguish the hypotheses we have outlined here. In Figure 10 in the Appendix D, we present mock observations with different spatial resolutions. We expect that an increase of a factor of two in spatial resolution will already marginally resolve the convective structure both in the radial velocity map and the intensity map, and be able to distinguish between all three scenarios.

An increase by a factor of two should be feasible. For ALMA, higher resolution can in principle already be achieved by going to higher frequencies. Asaki et al. (2023) reported to have achieved a spatial resolution of 5 mas for a carbon-rich AGB star, which is three times better. When ALMA upgrades its current 16 km baseline to 32 km, we can expect an (additional) improvement of a factor of two (Carpenter et al. 2020).

5. CONCLUSIONS

In this work, we investigate whether large-scale convection can affect the rotation measurement of Betelgeuse. We generate synthetic ALMA images from 3D CO5BOLD simulations of *non-rotating* RSGs, and compare them to the actual ALMA observations of Betelgeuse (K18). Our conclusions are summarised as follows:

- **Large-scale motions in the RSG atmospheres generated by convection can be mistaken for rotation in interferometric observations.** Both the convective cell size of the RSGs and the beam size used in ALMA observations are a large fraction of the stellar radius. Therefore, large-scale convection can be blurred as a dipolar feature in the radial velocity map that resembles rotation. This may apply to other cool stars, e.g. the $\sim 1 M_{\odot}$ AGB star R Dor, which is reported to be rotating at $v \sin i \sim 1 \text{ km s}^{-1}$ with ALMA (Figure 1 in Vlemmings et al. 2018) but only displays turbulent motions in higher-resolution VLTI/AMBER observations probing similar heights above the photosphere (Figure 7 in Ohnaka et al. 2019).
- **Future interferometric observations, e.g. with ALMA, are needed to assess the rotation of Betelgeuse.** Our simulations suggest that another single-epoch observation of Betelgeuse with ALMA is sufficient to confirm if the observed maps show signs of rotation. Multi-epoch observations and higher spatial resolutions are desired for further constraints.
- **The post-processing package developed in this work can be applied to other forward modelings from 3D simulations of (binary) cool stars to synthetic radio spectra (e.g. Ramstedt et al. 2017; Doan et al. 2020; De Ceuster et al. 2022).** This is particularly timely with the ongoing ALMA programs such as DEATHSTAR (Ramstedt et al. 2020; Andriantsaralaza et al. 2021) and ATOMIUM (Decin et al. 2020; Gottlieb et al. 2022; Montargès et al. 2023; Decin et al. 2023) that advance our understanding of chemistry, dust formation, planetary nebulae, binary interaction, and mass loss of these cool stars.
- **Regardless of whether Betelgeuse is rapidly rotating, more efforts are needed in both theoretical and observational aspects of RSGs.** If Betelgeuse is indeed rapidly rotating, understanding the consequences of convection may well still be important for accurately interpreting the observational signatures of rotation. The stellar merger scenario for the rapid rotation (Wheeler et al. 2017; Chatzopoulos et al. 2020; Sullivan et al. 2020; Shiber et al. 2023) would demand further studies in the context of Betelgeuse’s other properties, e.g. its runaway nature (Harper et al. 2008; Decin et al. 2012). If, on the other hand, future observations show evidence of turbulent motions, it may be possible for ALMA and other interferometers to trace the velocity field in different heights across the RSG atmosphere. Such observations would enable us to investigate the possible connections between pulsation, convection, and wind-launching mechanisms (Yoon & Cantiello 2010; Kee et al. 2021).

We acknowledge helpful discussions with Pierre Kervella, Norbert Langer and Falk Herwig. A.C. acknowledges support from the French National Research Agency (ANR) funded project PEPPER (ANR-20-CE31-0002). B.F. has received funding from the European Research Council (ERC) under the European Union’s Horizon 2020 research and innovation programme (Grant agreement No. 883867, project EXWINGS). The CO5BOLD simulations were enabled by resources provided by the Swedish National Infrastructure for Computing (SNIC) and PSMN in Lyon, France. This research project was partly conducted using computational resources (and/or scientific computing services) at the Max-Planck Computing & Data Facility. This research was supported by the Munich Institute for Astro-, Particle and BioPhysics (MIAPbP) which is funded by the Deutsche Forschungsgemeinschaft (DFG, German Research Foundation) under Germany’s Excellence Strategy – EXC-2094 – 390783311.

Software: CO5BOLD (Freytag et al. 2012), FASTCHEM2 (Stock et al. 2018, 2022), MARCS (Gustafsson et al. 2008), MAGRITTE (De Ceuster et al. 2020a,b, 2022), MESA (Paxton et al. 2011, 2013, 2015, 2018, 2019; Jermyn et al. 2023), Astropy (Astropy Collaboration et al. 2013, 2018, 2022), NumPy (Harris et al. 2020), SciPy (Virtanen et al. 2020), Matplotlib (Hunter 2007), Jupyter (Kluyver et al. 2016)

APPENDIX

A. SINGLE STAR 1D MODELS

The fast rotation rate inferred for Betelgeuse by K18 is surprising in light of the predictions of single-star models (Wheeler et al. 2017; Chatzopoulos et al. 2020). We illustrated this in Figure 1 mentioned briefly in the main text. Here we provide additional details.

We show predictions for massive star evolutionary models. During their main-sequence evolution (core H burning, blue shading), massive stars rotate up to a few hundred km s^{-1} , but once they have expanded to become RSGs (core He burning, red shading) their rotation rates drop to 0.1-0.001 km s^{-1} . In general, the RSGs with higher initial masses rotate slower due to higher angular momentum loss via stronger stellar wind.

The inferred rotation rate for Betelgeuse is 2-3 orders of magnitude larger than what is predicted, violating the expectations for single-star evolution. The figure shows the measurement for Betelgeuse by K18 as a red box. The bottom of the box corresponds to an assumed orientation where we see the star equator on ($i = 90^\circ$). The center of the box assumes $\langle \sin i \rangle = \pi/4$, which corresponds to the average for random orientations. The top of the box assumes $i = 20^\circ$, which is the value originally suggested by Uitenbroek et al. (1998) based on the location of the hot spot.

The models shown are computed with 1D stellar evolution code MESA v22.05.1 (Paxton et al. 2011, 2013, 2015, 2018, 2019; Jermyn et al. 2023), with initial masses of 12, 15, 18, 21 M_\odot and initial rotational velocities of 100, 200, 300 km s^{-1} at metallicity $Z = 0.02$. Convection is modelled according to mixing-length theory with $\alpha_{\text{MLT}} = 1.5$, plus an exponential overshoot scheme (Herwig 2000) with coefficients $f_{\text{ov}} = 0.0415$ and $f_{0,\text{ov}} =$

0.008 (Brott et al. 2011). The convective boundary is determined with the Ledoux (1947) criterion, and we assume efficient semiconvection (Langer et al. 1983, 1985). During the main sequence, wind mass loss is accounted for as in Vink et al. (2001), while we switch to de Jager et al. (1988) when the effective temperature drops below 10^4 K. We include the following mechanisms of rotational mixing and angular momentum transport (see Heger et al. 2000; Paxton et al. 2013): dynamical shear instability, secular shear instability, Eddington-Sweet circulation, Goldreich-Schubert-Fricke instability and Spruit-Tayler dynamo (Spruit 2002; Heger et al. 2005; Paxton et al. 2013).

B. ORDER-OF-MAGNITUDE ESTIMATES

In this section, we estimate the properties of convection of RSGs with order-of-magnitude analytical arguments. The surface convective cell size is determined by the effective temperature T_{eff} and surface gravity g . The convective velocity, on the other hand, is determined by T_{eff} alone. These parameters can be estimated on the order-of-magnitude level, given our understanding of RSGs and measured properties of Betelgeuse.

Near the photosphere, the horizontal size d of the convective cell can be estimated from the pressure scale height H_p multiplied by a factor α of order 10 for RSGs (Tremblay et al. 2013; Paladini et al. 2018). Therefore, the surface convective cell size is

$$d \sim \alpha \frac{k_{\text{B}} T_{\text{eff}}}{\mu m_{\text{u}} g} \sim 66 R_\odot \left(\frac{\alpha}{10} \right) \left(\frac{T_{\text{eff}}}{3600 \text{ K}} \right) \left(\frac{g}{\text{g cm}^{-3}} \right)^{-1}, \quad (\text{B1})$$

where k_{B} is the Boltzmann constant, m_{u} is the proton mass, μ is the mean molecular weight taken to be

0.643 for near solar composition. A similar method was also adopted to estimate the size of granules in 3D CO5BOLD RSG simulations (Chiavassa et al. 2011b). This estimate indicates that the surface convective cell size could be $\sim 10\%$ of the stellar radius within the uncertainties of parameters measured for Betelgeuse (Dolan et al. 2016; Joyce et al. 2020).

The convective velocity v_c in the RSG envelope can be estimated by equating the energy flux to the convective flux:

$$v_c \sim \sqrt[3]{\frac{\sigma_{\text{SB}} T_{\text{eff}}^4}{\rho_s}} \sim 21 \text{ km s}^{-1} \left(\frac{T_{\text{eff}}}{3600 \text{ K}} \right)^{\frac{4}{3}} \rho_{s,-9}^{-\frac{1}{3}}, \quad (\text{B2})$$

where σ_{SB} is the Stefan-Boltzmann constant and $\rho_{s,-9}$ is the surface density in units of $10^{-9} \text{ g cm}^{-3}$ (representative density taken from the MESA models; see also Figure 2 of Goldberg et al. 2022). The constants of order unity are omitted here.

The timescale for the surface convective structure to readjust can be estimated as

$$t_{\text{surf}} \sim \frac{d}{v_c} \sim 25 \text{ days} \left(\frac{\alpha}{10} \right) \left(\frac{T_{\text{eff}}}{3600 \text{ K}} \right)^{-\frac{1}{3}} \left(\frac{g}{\text{g cm}^{-3}} \right)^{-1} \rho_{s,-9}^{\frac{1}{3}}, \quad (\text{B3})$$

typically at the order of weeks to months.

In comparison, the velocity field is predicted to be influenced by the deep convection, which operates over a larger length scale comparable to the stellar radius as shown in 3D simulations (Kravchenko et al. 2019). The timescale for the deep convection can thus be estimated as the convective turnover timescale

$$t_{\text{turnover}} \sim \frac{R}{v_c} \sim 0.8 \text{ yrs} \left(\frac{R}{800 R_{\odot}} \right) \left(\frac{T_{\text{eff}}}{3600 \text{ K}} \right)^{-\frac{4}{3}} \rho_{s,-9}^{\frac{1}{3}}. \quad (\text{B4})$$

C. POST-PROCESSING PACKAGE: METHODS, TESTS, AND LIMITATIONS

C.1. Equilibrium chemistry with FASTCHEM2

The number densities of different species in our simulations are obtained from FASTCHEM2 assuming chemical equilibrium. On-the-fly calculations are time-consuming given the large number of grid points and snapshots in the simulations. Therefore, we pre-calculate the number density tables using FASTCHEM2 that cover the parameter space of $2.5 \leq \log_{10}(T/[\text{K}]) \leq 5.5$, $-30 \leq \log_{10}(\mathcal{R}) \leq -9$ where $\mathcal{R} = (P/[\text{dyn cm}^{-2}])/(T/[\text{K}])^4$. Here, T is the gas temperature and P is the gas pressure. The number densities in our simulations are interpolated values from these tables. To verify that the interpolated results from the pre-calculated FASTCHEM2 table are suitable for RSG simulations, we compare the interpolated values to the values given by a MARCS RSG model in Figure 5. The MARCS code was developed to create 1D

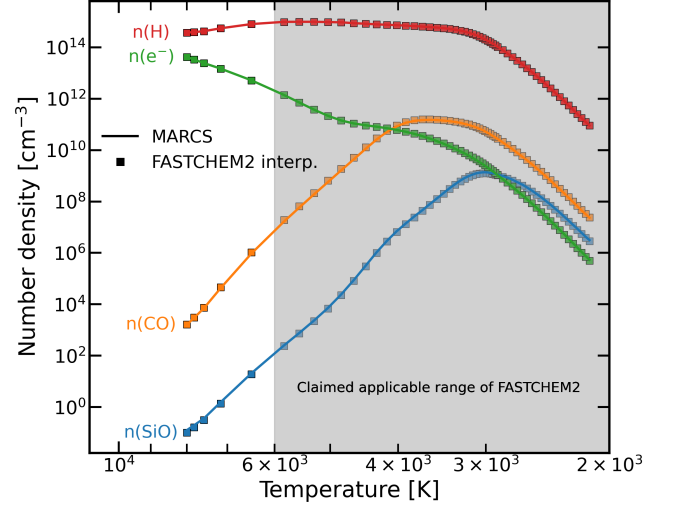


Figure 5. Comparison of number densities from interpolated results of pre-calculated FASTCHEM2 table (squares) against those from MARCS (curves). The colors indicate the number densities of atomic hydrogen, electrons, CO molecules, and SiO molecules, respectively.

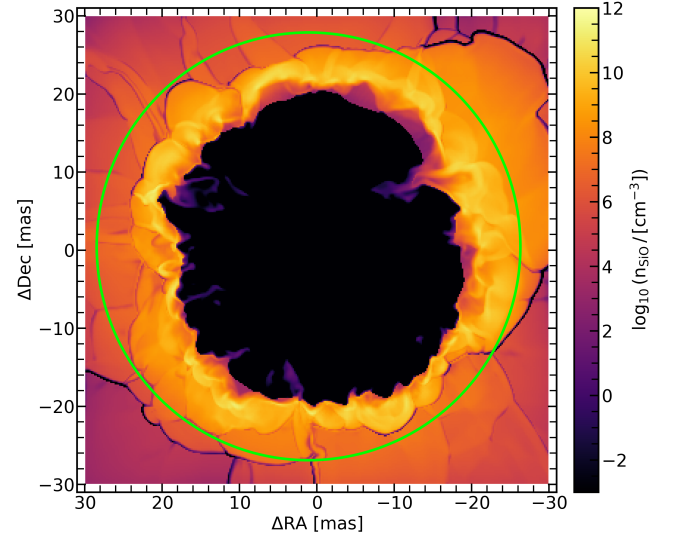


Figure 6. 2D middle slice of SiO number density in the simulated RSG envelope. The green circle is the radio photosphere of the star. From the same snapshot of the simulation shown in Figure 2.

atmospheric models for evolved stars (Gustafsson et al. 2008), which has been widely used to produce spectra to obtain basic parameters of RSGs from spectroscopy (e.g. Levesque et al. 2005). The interpolated FASTCHEM2 values closely agree with the MARCS values.

In Figure 6, we show an example of the SiO number density distribution in our simulations by taking a 2D slice along the middle cross-section. The light green circle indicates the radio photosphere determined by the

continuum intensity map (see Section 2.2). In our simulations, molecules are dissociated in the inner envelope due to high temperature. The most abundant SiO molecules are found near the optical photosphere due to recombination. The presence of shocks outside of the photosphere can be seen from the SiO number density slice.

C.2. Continuum and line radiative transfer

In our post-processing, we numerically integrate the time-independent radiative transfer equation along the ray neglecting scattering. A distance x can be defined from the origin of the ray. The optical depth is

$$\tau_\nu(\hat{\mathbf{n}}, \mathbf{r}) \equiv \int_0^{x(\hat{\mathbf{n}}, \mathbf{r})} \chi_\nu dx'. \quad (\text{C5})$$

Here, $\hat{\mathbf{n}}$ is the unit vector along the ray direction, and \mathbf{r} is the vector of position. The intensity can then be calculated as

$$I_\nu(x) = I_\nu(0)e^{-\tau_\nu} + \int_{e^{-\tau_\nu}}^1 S_\nu(\tau_\nu - \tau'_\nu) d(e^{-\tau'_\nu}), \quad (\text{C6})$$

where S_ν is the source function defined by $S_\nu \equiv \eta_\nu/\chi_\nu$. I_ν , η_ν , χ_ν are the intensity, emissivity, and opacity at frequency ν . The intensity $I_\nu(0)$ at the origin is taken to be zero.

For the wavelength range studied here, the emissivity and opacity are contributed by continuum emission and molecular lines, namely $\eta_\nu = \eta_\nu^{\text{con}} + \eta_\nu^{\text{line}}$, $\chi_\nu = \chi_\nu^{\text{con}} + \chi_\nu^{\text{line}}$. We assume that $\eta_\nu^{\text{con}} = \chi_\nu^{\text{con}} B_\nu$, where B_ν is the Planck function. The continuum opacity χ_ν^{con} , dominated by H^- free-free transitions, is taken from the analytical fits in Harper et al. (2001) specifically made for radio observations of Betelgeuse. Relevant quantities for ^{28}SiO ($\nu = 2, J = 8 - 7$) lines are obtained from the ExoMol database² (Tennyson & Yurchenko 2012; Tennyson et al. 2016) using the results of Yurchenko et al. (2022), and further computed assuming local thermal equilibrium (LTE). The line emissivity and opacity contributed by the transition from level i to level j are computed following standard assumptions (e.g. De Ceuster et al. 2020a):

$$\eta_\nu^{\text{line}, ij} = \frac{h\nu}{4\pi} n_i A_{ij} \phi_\nu^{ij}, \quad (\text{C7})$$

$$\chi_\nu^{\text{line}, ij} = \frac{h\nu}{4\pi} (n_j B_{ji} - n_i B_{ij}) \phi_\nu^{ij}, \quad (\text{C8})$$

where h is the Planck constant, n_i is the number density of the species at level i , and A_{ij} , B_{ij} are Einstein coefficients. The line profile function is assumed to be a Gaussian with a line width contributed by thermal broadening

$$\phi_\nu^{ij} = \frac{1}{\delta\nu_{ij}\sqrt{\pi}} \exp\left[-\left(\frac{\nu - \tilde{\nu}_{ij}}{\delta\nu_{ij}}\right)^2\right], \quad (\text{C9})$$

² <https://www.exomol.com>

$$\delta\nu_{ij} = \frac{|v_{\text{therm}}|}{c} \tilde{\nu}_{ij}, \quad (\text{C10})$$

where the Doppler-shifted frequency $\tilde{\nu}_{ij}$ and the thermal velocity v_{therm} are

$$\tilde{\nu}_{ij} = \nu_{ij} \left(1 - \frac{\hat{\mathbf{n}} \cdot \mathbf{v}}{c}\right), \quad (\text{C11})$$

$$v_{\text{therm}} = \sqrt{\frac{2k_B T}{m}}. \quad (\text{C12})$$

Here, ν_{ij} is the rest frequency for the transition, \mathbf{v} is the local velocity, c is the speed of light, T is the gas temperature, and m is the particle mass of the species. The Doppler shift follows the convention that velocity towards the observer is blue-shifted and has negative values.

We have tested our algorithm against the line transfer code MAGRITTE (De Ceuster et al. 2020a,b, 2022) by applying both of them to the CO5BOLD simulation snapshot. The results agree with each other. However, MAGRITTE needs to construct the Voronoi grid. In comparison, our method runs faster with CO5BOLD snapshots which are computed on a Cartesian grid, and does not suffer from extra interpolation errors. Additionally, MAGRITTE has not yet incorporated continuum opacity or interface to the ExoMol database, both of which are important for this study.

C.3. Gaussian line fit and rotation measurement

An example of our Gaussian line fit procedure is illustrated in Figure 7. Green arrows connect the line profiles to their corresponding pixels (indicated in black). To obtain the radial velocity map, we fit a Gaussian (orange solid line) to the line profile (blue solid line) in each pixel of the image, and find the mean value of the Gaussian (orange dotted line).

Following Section 3.5 in K18, we subtract the inferred systematic velocity from the radial velocity map, and fit a projected radial velocity map of a rigidly rotating sphere to the synthesized map. Namely, we assume that the v_{sys} -subtracted radial velocity map has the velocity distribution of $v(x, y) = v \sin i \times (x \cos \theta + y \sin \theta)/R_{\text{star}}$, where the fitted parameters are the position angle θ and the inferred $v \sin i$, and x, y are the coordinates of the 2D radial velocity map.

Instead of using the radio photospheric radius R_{star} for the fit, we suggest it is more consistent with the physical scenario to use the radius $R_{\text{shell}} \approx 1.3R_{\text{star}}$ of the molecular shell probed by ALMA. This would increase the measured $v \sin i$ at the molecular shell by a factor of 1.3, i.e., $v \sin i_{\text{shell}} \approx 7 \text{ km s}^{-1}$ at the molecular shell. Assuming that the molecular shell co-rotates with the radio photosphere, this translates to a rotational velocity at the radio photosphere a factor of 1.3 less than the value measured at the molecular shell, i.e., $v \sin i_{\text{radio}} \approx 5.5 \text{ km s}^{-1}$ at the radio photosphere. However, if the molecular shell and the radio photosphere are not fully coupled, e.g. assuming similar specific angular momentum between the molecular shell and the

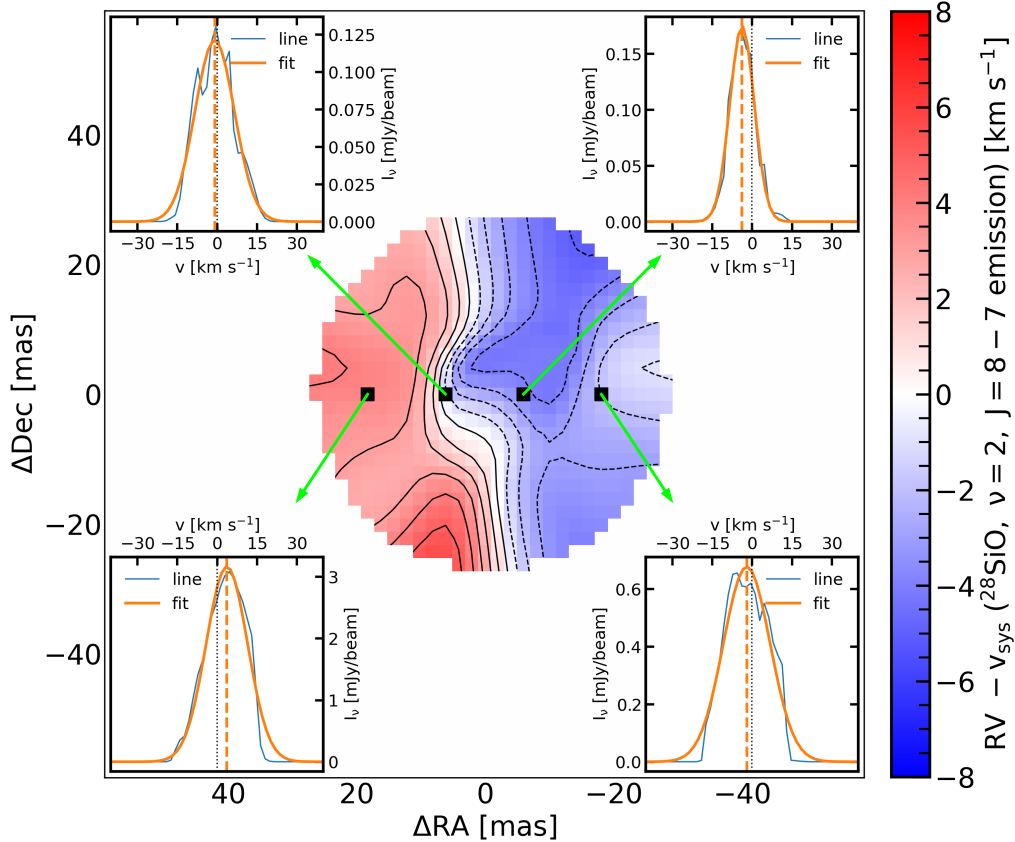


Figure 7. Examples of emission line profiles from synthetic ALMA images. Four small subplots show the simulated line profiles (blue) and fitted Gaussian (orange) in four pixels (shaded in black) of the synthetic ALMA image. In each pixel, the mean value (orange dashed vertical line) of the fitted Gaussian is taken to be the radial velocity from the Doppler shift. From the same snapshot of the simulation shown in Figure 2.

radio photosphere, then the rotational velocity at the radio photosphere would be another factor of 1.3 higher, namely $v \sin i_{\text{radio}} \approx 9 \text{ km s}^{-1}$ at the radio photosphere. Since the optical photosphere is yet another factor of 1.3 smaller than the radio photosphere, the measurement by K18 would give $v \sin i_{\text{optical}} \approx 4 \text{ km s}^{-1}$ at the optical photosphere assuming constant angular frequency (co-rotation) outside the star, or $v \sin i_{\text{optical}} \approx 12 \text{ km s}^{-1}$ assuming constant specific angular momentum outside the star. In this work, we closely follow the procedure done by K18 for direct comparison, and thus use R_{star} for the rotation fit, with the underlying assumption that the molecular shell co-rotates with the radio photosphere.

C.4. Limitations

We scale the simulation such that it has an inferred radio photospheric radius R_{star} of $\sim 30 \text{ mas}$. However, this corresponds to a distance of 130 pc, consistent with the original *Hipparcos* parallax (131_{-23}^{+35} ; ESA 1997; Perryman et al. 1997) and its revised value (152_{-17}^{+22} ; Van Leeuwen 2007) but much closer than the distance derived from *Hipparcos* data combined with radio observations (197_{-35}^{+55} ; Harper et al. 2008) and its revised value

(222_{-34}^{+48} ; Harper et al. 2017). This is partly because the default simulation used in this work has a smaller radius than Betelgeuse, and therefore needs to be placed closer to get a similar parallax. Another reason is rooted in the limitations of the 3D models, which have been shown to be less extended than actual RSGs (Arroyo-Torres et al. 2015; Climent et al. 2020; Chiavassa et al. 2022). This could be due to the fact that the radiation pressure is not included in the simulations (Freytag et al. 2012).

The simulated continuum intensity is about half of the observed value (see Figure 2), and the line amplitude is an order of magnitude lower than observed (see Figure 7 compared to Figure 1 and 9 in K18). This could result from the small atmospheric extension of the simulations, or not including non-equilibrium chemistry, non-LTE populations, dust emission, maser, or scattering in the post-processing. However, as we are interested in the radial velocity shifts instead of the molecular abundances in this study, the effects of these missing physics are expected to be limited. This is supported by our simulations, which show no significant variations in the velocity field from the surface to the molecular layer.

Table 2. Parameters of the CO5BOLD simulations taken from [Ahmad et al. \(2023\)](#), compared to the observed values for Betelgeuse. The stellar parameters for both simulations and observations are listed as surface gravity $\log_{10} g$, effective temperature T_{eff} , luminosity $\log_{10} L_*$, and radius R_* . All these surface quantities in simulations are taken at the local minimum point of specific entropy averaged over spherical shells and time, as described in [Ahmad et al. \(2023\)](#). We also list the mass M_{pot} used for the gravitational potential and envelope mass M_{env} for the simulations. The convective turnover timescale t_{turnover} is estimated analytically as R_*/v_c , where the convective velocity v_c are calculated using the equations in Appendix B. The number of grid cells, simulation box size x_{box} , number of snapshots, and the physical time t_{snap} covered by the extracted snapshots are listed in sequence.

		$\log_{10} g$ [cm s^{-2}]	T_{eff} [K]	$\log_{10} L_*$ [L_{\odot}]	R_* [R_{\odot}]	M_{pot} [M_{\odot}]	M_{env} [M_{\odot}]	t_{turnover} [yr]	Grid [#]	x_{box} [R_{\odot}]	Snapshot [#]	t_{snap} [yr]
Sim.	default (st35gm04n37)	-0.419	3366	4.62	597	5.0	0.5	~ 0.7	315 ³	1626	80	5.1
	B (st35gm03n020)	-0.246	3620	4.95	759	12.0	3.0	~ 0.8	637 ³	2093	100	6.3
Obs.	Betelgeuse	-0.5 ^a	3500 ⁺²⁰⁰ ₋₂₀₀ ^b	5.10 ^{+0.22} _{-0.22} ^c	764 ⁺¹¹⁶ ₋₆₂ ^d	-	-	-	-	-	-	-

^aLobel & Dupree (2000)

^bDolan et al. (2016) (chosen value motivated by multiple sources)

^cHarper et al. (2008)

^dJoyce et al. (2020)

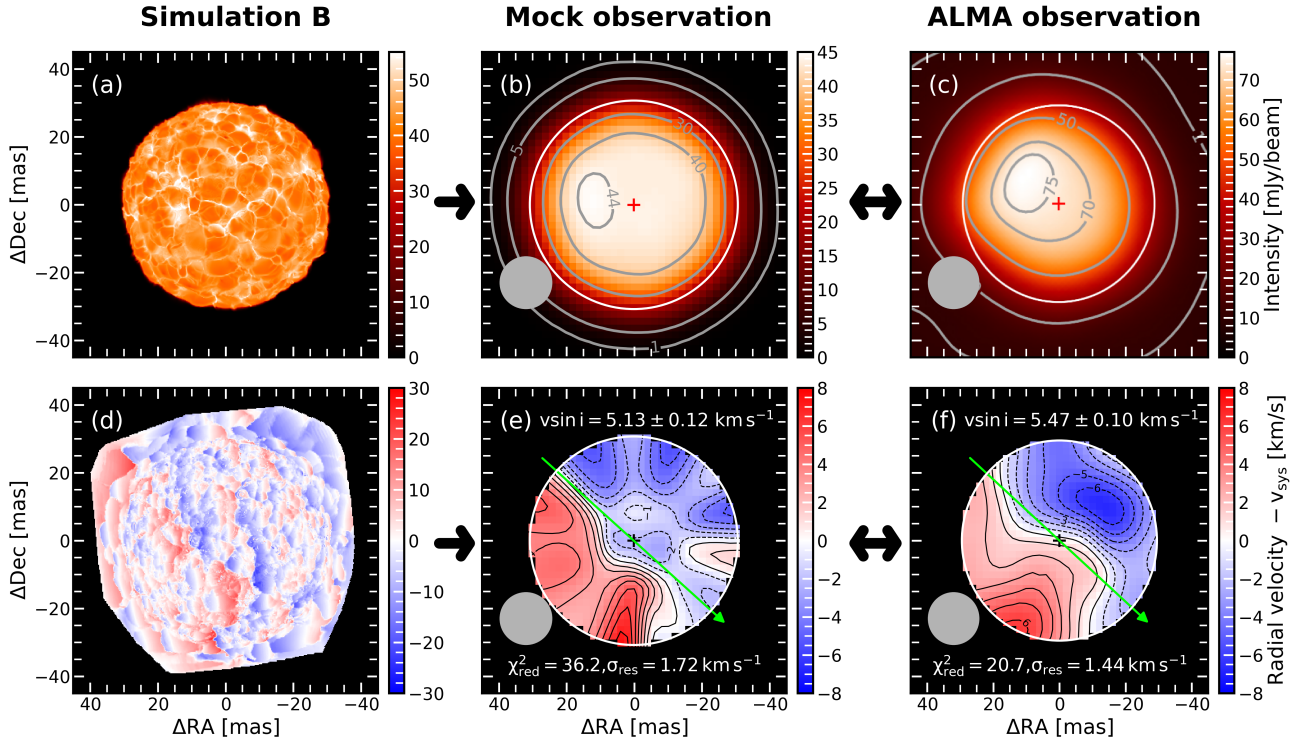


Figure 8. Continuum intensity map and radial velocity map of best-fit simulation B snapshot, compared with ALMA observations of Betelgeuse. Physical quantities marked in white are defined the same way as in Table 1 using the method in Section 2.3. Credit for the right two panels: Kervella et al., A&A, 609, A67, 2018, reproduced with permission © ESO.

A more uncertain aspect is whether the convective structure in our simulations can represent actual RSG convection. The convective length scales are subject to

uncertainties of stellar parameters of Betelgeuse itself, as well as the resolution of the simulations ([Chiavassa et al. 2011a](#)). Aside from that, core convection simu-

lations suggest that large-scale convection is dominated by dipolar flows (see, e.g. [Lecoanet & Edelmann 2023](#), for a review), which are specifically damped in our simulations by the drag forces in the central region ([Freytag et al. 2012](#)). However, we expect that an enhancement in the dipolar flows would only make our argument stronger.

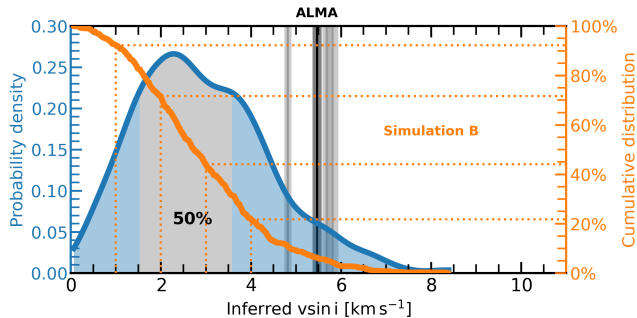


Figure 9. Probability distribution of apparent $v \sin i$, similar to Figure 3 but inferred from simulation B.

D. ADDITIONAL SIMULATIONS

D.1. Impact of the chosen stellar parameters

The parameters of two sets of 3D simulations used in this study are shown in Table 2. The default simulation is discussed in the main text (Figure 2 and Figure 3), while an alternative simulation with smaller surface granules is presented in Figure 8 and Figure 9. Due to the small granule size compared to the ALMA beam size, the radial velocity map displays small-scale features (Figure 8) and therefore is less likely to be mistaken for rotation (Figure 9). The change in the intensity map, however, is less obvious. In particular, its radial velocity map shows a velocity magnitude similar to the default simulation, but with more cell-like structures. This indicates that the magnitude of velocity in the radial velocity map may be only determined by the maximum convective velocity and the relative beam size, and not sensitive to the cell size. The morphology of the radial velocity map, however, is sensitive to the cell size, and consequently to the surface gravity.

D.2. Impact of the beam size

To further explore the importance of the beam size relative to the surface granule size, we vary the beam size in the mock observations for the default simulation. In Figure 10, we show that, as the spatial resolution of the interferometer increases, more small-scale features can be revealed in both the intensity map and the radial velocity map. As shown in the third column (c & g), decreasing the beam size by a factor of two would already help to marginally resolve the convective structure, both in the radial velocity map and the intensity map. On the contrary, increasing the beam size by a

factor of two (a & e) smears out any asymmetrical feature in the intensity map, and the radial velocity map is completely dominated by a dipolar pattern. Strikingly, as the spatial resolution of the interferometer increases (left to right), the measured radio photospheric radius monotonically decreases from ~ 30 mas to ~ 25 mas, whilst the peak magnitude of radial velocity monotonically increases from ~ 6 to ~ 30 km s^{-1} . As a result of increasing radial velocity magnitude, the fitted $v \sin i$, χ_{red}^2 , and σ_{res} all increase with higher resolution, among which χ_{red}^2 increases by three orders of magnitude. If future observations can be done with higher resolution, these are the clear signatures to look for to support our hypothesis.

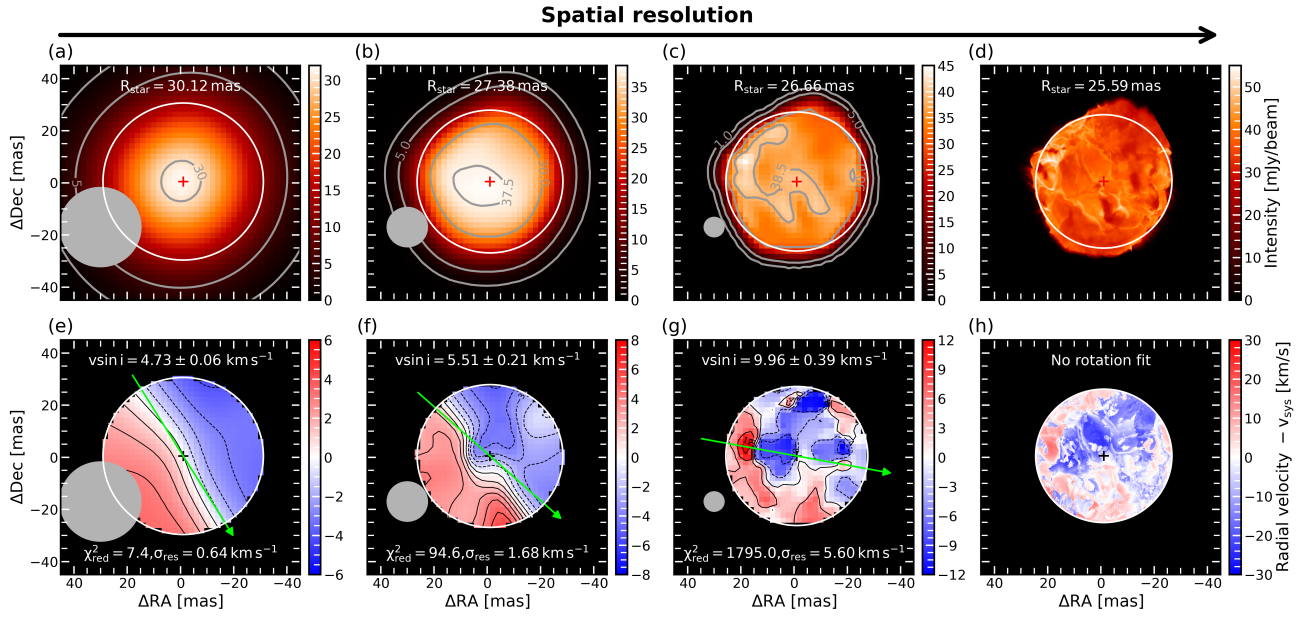


Figure 10. Effects of spatial resolution on the observed intensity map and radial velocity map in mock observations. From the left to the right, spatial resolution increases with decreasing beam size (indicated by grey circles). The second column (b & f) uses the standard resolution of FWHM = 18 mas adopted in ALMA observations of Betelgeuse (K18), the same as shown in Figure 2. In comparison, the beam size of the first column (a & e) is increased by a factor of two (36 mas), whereas the beam size of the third column (c & g) is reduced by a factor of two (9 mas). The last column (d & h) is the same original simulation image shown in Figure 2. Physical quantities marked in white are defined the same way as in Table 1 using the method in Section 2.3.

REFERENCES

- Agúndez, M., Martínez, J. I., de Andres, P. L., Cernicharo, J., & Martín-Gago, J. A. 2020, *A&A*, 637, A59, doi: [10.1051/0004-6361/202037496](https://doi.org/10.1051/0004-6361/202037496)
- Ahmad, A., Freytag, B., & Höfner, S. 2023, *A&A*, 669, A49, doi: [10.1051/0004-6361/202244555](https://doi.org/10.1051/0004-6361/202244555)
- Andriantsaralaza, M., Ramstedt, S., Vlemmings, W. H. T., et al. 2021, *A&A*, 653, A53, doi: [10.1051/0004-6361/202140952](https://doi.org/10.1051/0004-6361/202140952)
- Antoni, A., & Quataert, E. 2022, *MNRAS*, 511, 176, doi: [10.1093/mnras/stab3776](https://doi.org/10.1093/mnras/stab3776)
- Ariste, A. L., Georgiev, S., Mathias, P., et al. 2022, *A&A*, 661, A91, doi: [10.1051/0004-6361/202142271](https://doi.org/10.1051/0004-6361/202142271)
- Ariste, A. L., Mathias, P., Tessore, B., et al. 2018, *A&A*, 620, A199, doi: [10.1051/0004-6361/201834178](https://doi.org/10.1051/0004-6361/201834178)
- Arroyo-Torres, B., Wittkowski, M., Chiavassa, A., et al. 2015, *A&A*, 575, A50, doi: [10.1051/0004-6361/201425212](https://doi.org/10.1051/0004-6361/201425212)
- Asaki, Y., Maud, L. T., Francke, H., et al. 2023, ALMA High-frequency Long Baseline Campaign in 2021: Highest Angular Resolution Submillimeter Wave Images for the Carbon-rich Star R Lep, doi: [10.48550/arXiv.2310.09664](https://doi.org/10.48550/arXiv.2310.09664)
- Astropy Collaboration, Robitaille, T. P., Tollerud, E. J., et al. 2013, *A&A*, 558, A33, doi: [10.1051/0004-6361/201322068](https://doi.org/10.1051/0004-6361/201322068)
- Astropy Collaboration, Price-Whelan, A. M., Sipőcz, B. M., et al. 2018, *AJ*, 156, 123, doi: [10.3847/1538-3881/aabc4f](https://doi.org/10.3847/1538-3881/aabc4f)
- Astropy Collaboration, Price-Whelan, A. M., Lim, P. L., et al. 2022, *ApJ*, 935, 167, doi: [10.3847/1538-4357/ac7c74](https://doi.org/10.3847/1538-4357/ac7c74)
- Barnbaum, C., Morris, M., & Kahane, C. 1995, *ApJ*, 450, 862, doi: [10.1086/176190](https://doi.org/10.1086/176190)
- Brott, I., de Mink, S. E., Cantiello, M., et al. 2011, *A&A*, 530, A115, doi: [10.1051/0004-6361/201016113](https://doi.org/10.1051/0004-6361/201016113)
- Brun, A. S., & Palacios, A. 2009, *ApJ*, 702, 1078, doi: [10.1088/0004-637X/702/2/1078](https://doi.org/10.1088/0004-637X/702/2/1078)
- Brun, A. S., & Toomre, J. 2002, *ApJ*, 570, 865, doi: [10.1086/339228](https://doi.org/10.1086/339228)
- Brunner, M., Mecina, M., Maercker, M., et al. 2019, *A&A*, 621, A50, doi: [10.1051/0004-6361/201833652](https://doi.org/10.1051/0004-6361/201833652)
- Carlberg, J. K., Cunha, K., Smith, V. V., & Majewski, S. R. 2012, *ApJ*, 757, 109, doi: [10.1088/0004-637X/757/2/109](https://doi.org/10.1088/0004-637X/757/2/109)
- Carpenter, J., Iono, D., Kemper, F., & Wootten, A. 2020, The ALMA Development Program: Roadmap to 2030, doi: [10.48550/arXiv.2001.11076](https://doi.org/10.48550/arXiv.2001.11076)
- Chatzopoulos, E., Frank, J., Marcello, D. C., & Clayton, G. C. 2020, *ApJ*, 896, 50, doi: [10.3847/1538-4357/ab91bb](https://doi.org/10.3847/1538-4357/ab91bb)
- Chiavassa, A., Freytag, B., Masseron, T., & Plez, B. 2011a, *A&A*, 535, A22, doi: [10.1051/0004-6361/201117463](https://doi.org/10.1051/0004-6361/201117463)
- Chiavassa, A., Haubois, X., Young, J. S., et al. 2010, *A&A*, 515, A12, doi: [10.1051/0004-6361/200913907](https://doi.org/10.1051/0004-6361/200913907)
- Chiavassa, A., Kravchenko, K., & Goldberg, J. A. 2024, *Living Reviews in Computational Astrophysics*, submitted
- Chiavassa, A., Plez, B., Josselin, E., & Freytag, B. 2009, *A&A*, 506, 1351, doi: [10.1051/0004-6361/200911780](https://doi.org/10.1051/0004-6361/200911780)
- Chiavassa, A., Pasquato, E., Jorissen, A., et al. 2011b, *A&A*, 528, A120, doi: [10.1051/0004-6361/201015768](https://doi.org/10.1051/0004-6361/201015768)
- Chiavassa, A., Kravchenko, K., Montargès, M., et al. 2022, *A&A*, 658, A185, doi: [10.1051/0004-6361/202142514](https://doi.org/10.1051/0004-6361/202142514)
- Climont, J. B., Wittkowski, M., Chiavassa, A., et al. 2020, *A&A*, 635, A160, doi: [10.1051/0004-6361/201936734](https://doi.org/10.1051/0004-6361/201936734)
- De Ceuster, F., Homan, W., Yates, J., et al. 2020a, *MNRAS*, 492, 1812, doi: [10.1093/mnras/stz3557](https://doi.org/10.1093/mnras/stz3557)
- De Ceuster, F., Bolte, J., Homan, W., et al. 2020b, *MNRAS*, 499, 5194, doi: [10.1093/mnras/staa3199](https://doi.org/10.1093/mnras/staa3199)
- De Ceuster, F., Ceulemans, T., Srivastava, A., et al. 2022, *JOSS*, 7, 3905, doi: [10.21105/joss.03905](https://doi.org/10.21105/joss.03905)
- de Jager, C., Nieuwenhuijzen, H., & van der Hucht, K. A. 1988, *A&AS*, 72, 259. <https://ui.adsabs.harvard.edu/abs/1988A%26AS...72..259D/abstract>
- de Mink, S. E., Sana, H., Langer, N., Izzard, R. G., & Schneider, F. R. N. 2014, *ApJ*, 782, 7, doi: [10.1088/0004-637X/782/1/7](https://doi.org/10.1088/0004-637X/782/1/7)
- Decin, L., Richards, A. M. S., Marchant, P., & Sana, H. 2023, ALMA detection of CO rotational line emission in red supergiant stars of the massive young star cluster RSGC1 – Determination of a new mass-loss rate prescription for red supergiants, doi: [10.48550/arXiv.2303.09385](https://doi.org/10.48550/arXiv.2303.09385)
- Decin, L., Cox, N. L. J., Royer, P., et al. 2012, *A&A*, 548, A113, doi: [10.1051/0004-6361/201219792](https://doi.org/10.1051/0004-6361/201219792)
- Decin, L., Montargès, M., Richards, A. M. S., et al. 2020, *Science*, 369, 1497, doi: [10.1126/science.abb1229](https://doi.org/10.1126/science.abb1229)
- Doan, L., Ramstedt, S., Vlemmings, W. H. T., et al. 2020, *A&A*, 633, A13, doi: [10.1051/0004-6361/201935245](https://doi.org/10.1051/0004-6361/201935245)
- Dolan, M. M., Mathews, G. J., Lam, D. D., et al. 2016, *ApJ*, 819, 7, doi: [10.3847/0004-637X/819/1/7](https://doi.org/10.3847/0004-637X/819/1/7)
- Drevon, J., Millour, F., Cruzalèbes, P., et al. 2024, *MNRAS*, 527, L88, doi: [10.1093/mnras/slad138](https://doi.org/10.1093/mnras/slad138)
- ESA. 1997, ESA SP Series, Vol. 1200, The HIPPARCOS and TYCHO catalogues. Astrometric and photometric star catalogues derived from the ESA HIPPARCOS Space Astrometry Mission (Noordwijk, Netherlands: ESA Publications Division). <https://ui.adsabs.harvard.edu/abs/1997ESASP1200.....E>
- Freytag, B., Steffen, M., Ludwig, H. G., et al. 2012, *JCoPh*, 231, 919, doi: [10.1016/j.jcp.2011.09.026](https://doi.org/10.1016/j.jcp.2011.09.026)
- Gaulme, P., Jackiewicz, J., Spada, F., et al. 2020, *A&A*, 639, A63, doi: [10.1051/0004-6361/202037781](https://doi.org/10.1051/0004-6361/202037781)

- Gilliland, R. L., & Dupree, A. K. 1996, *ApJ*, 463, L29, doi: [10.1086/310043](https://doi.org/10.1086/310043)
- Goldberg, J. A., Jiang, Y.-F., & Bildsten, L. 2022, *ApJ*, 929, 156, doi: [10.3847/1538-4357/ac5ab3](https://doi.org/10.3847/1538-4357/ac5ab3)
- Gottlieb, C. A., Decin, L., Richards, A. M. S., et al. 2022, *A&A*, 660, A94, doi: [10.1051/0004-6361/202140431](https://doi.org/10.1051/0004-6361/202140431)
- Guinan, E., Wasatonic, R., Calderwood, T., & Carona, D. 2020, *The Astronomer's Telegram*, 13512, 1. <https://ui.adsabs.harvard.edu/abs/2020ATel13512....1G>
- Guinan, E. F., Wasatonic, R. J., & Calderwood, T. J. 2019, *The Astronomer's Telegram*, 13341, 1. <https://ui.adsabs.harvard.edu/abs/2019ATel13341....1G>
- Gustafsson, B., Edvardsson, B., Eriksson, K., et al. 2008, *A&A*, 486, 951, doi: [10.1051/0004-6361:200809724](https://doi.org/10.1051/0004-6361:200809724)
- Harper, G. M., & Brown, A. 2006, *ApJ*, 646, 1179, doi: [10.1086/505073](https://doi.org/10.1086/505073)
- Harper, G. M., Brown, A., & Guinan, E. F. 2008, *AJ*, 135, 1430, doi: [10.1088/0004-6256/135/4/1430](https://doi.org/10.1088/0004-6256/135/4/1430)
- Harper, G. M., Brown, A., Guinan, E. F., et al. 2017, *ApJ*, 154, 11, doi: [10.3847/1538-3881/aa6ff9](https://doi.org/10.3847/1538-3881/aa6ff9)
- Harper, G. M., Brown, A., & Lim, J. 2001, *ApJ*, 551, 1073, doi: [10.1086/320215](https://doi.org/10.1086/320215)
- Harris, C. R., Millman, K. J., van der Walt, S. J., et al. 2020, *Nature*, 585, 357, doi: [10.1038/s41586-020-2649-2](https://doi.org/10.1038/s41586-020-2649-2)
- Haubois, X., Perrin, G., Lacour, S., et al. 2009, *A&A*, 508, 923, doi: [10.1051/0004-6361/200912927](https://doi.org/10.1051/0004-6361/200912927)
- Heger, A., Langer, N., & Woosley, S. E. 2000, *ApJ*, 528, 368, doi: [10.1086/308158](https://doi.org/10.1086/308158)
- Heger, A., Woosley, S. E., & Spruit, H. C. 2005, *ApJ*, 626, 350, doi: [10.1086/429868](https://doi.org/10.1086/429868)
- Herwig, F. 2000, *A&A*, 360, 952, doi: [10.48550/arXiv.astro-ph/0007139](https://doi.org/10.48550/arXiv.astro-ph/0007139)
- Hunter, J. D. 2007, *Computing in Science and Engineering*, 9, 90, doi: [10.1109/MCSE.2007.55](https://doi.org/10.1109/MCSE.2007.55)
- Jadlovský, D., Krtička, J., Paunzen, E., & Štefl, V. 2023, *New Astronomy*, 99, 101962, doi: [10.1016/j.newast.2022.101962](https://doi.org/10.1016/j.newast.2022.101962)
- Jermyn, A. S., Bauer, E. B., Schwab, J., et al. 2023, *ApJS*, 265, 15, doi: [10.3847/1538-4365/aca8d](https://doi.org/10.3847/1538-4365/aca8d)
- Josselin, E., & Plez, B. 2007, *A&A*, 469, 671, doi: [10.1051/0004-6361:20066353](https://doi.org/10.1051/0004-6361:20066353)
- Joyce, M., Leung, S.-C., Molnár, L., et al. 2020, *ApJ*, 902, 63, doi: [10.3847/1538-4357/abb8db](https://doi.org/10.3847/1538-4357/abb8db)
- Kee, N. D., Sundqvist, J. O., Decin, L., Koter, A. d., & Sana, H. 2021, *A&A*, 646, A180, doi: [10.1051/0004-6361/202039224](https://doi.org/10.1051/0004-6361/202039224)
- Kervella, P., Decin, L., Richards, A. M. S., et al. 2018, *A&A*, 609, A67, doi: [10.1051/0004-6361/201731761](https://doi.org/10.1051/0004-6361/201731761)
- Kitzmann, D., Hoeijmakers, H. J., Grimm, S. L., et al. 2023, *A&A*, 669, A113, doi: [10.1051/0004-6361/202142969](https://doi.org/10.1051/0004-6361/202142969)
- Kitzmann, D., Heng, K., Rimmer, P. B., et al. 2018, *ApJ*, 863, 183, doi: [10.3847/1538-4357/aace5a](https://doi.org/10.3847/1538-4357/aace5a)
- Kluyver, T., Ragan-Kelley, B., Pérez, F., et al. 2016, in *Positioning and Power in Academic Publishing: Players, Agents and Agendas* (IOS Press), doi: [10.3233/978-1-61499-649-1-87](https://doi.org/10.3233/978-1-61499-649-1-87)
- Kochanek, C. S., Adams, S. M., & Belczynski, K. 2014, *MNRAS*, 443, 1319, doi: [10.1093/mnras/stu1226](https://doi.org/10.1093/mnras/stu1226)
- Kravchenko, K., Chiavassa, A., Eck, S. V., et al. 2019, *A&A*, 632, A28, doi: [10.1051/0004-6361/201935809](https://doi.org/10.1051/0004-6361/201935809)
- Kravchenko, K., Jorissen, A., Van Eck, S., et al. 2021, *A&A*, 650, L17, doi: [10.1051/0004-6361/202039801](https://doi.org/10.1051/0004-6361/202039801)
- Langer, N., El Eid, M. F., & Fricke, K. J. 1985, *A&A*, 145, 179. <https://ui.adsabs.harvard.edu/abs/1985A&A...145..179L>
- Langer, N., Fricke, K. J., & Sugimoto, D. 1983, *A&A*, 126, 207. <https://ui.adsabs.harvard.edu/abs/1983A&A...126..207L/abstract>
- Lau, M. Y. M., Cantiello, M., Jermyn, A. S., et al. 2022, *Hot Jupiter engulfment by a red giant in 3D hydrodynamics*, doi: [10.48550/arXiv.2210.15848](https://doi.org/10.48550/arXiv.2210.15848)
- Lecoanet, D., & Edelman, P. V. F. 2023, *Galaxies*, 11, 89, doi: [10.3390/galaxies11040089](https://doi.org/10.3390/galaxies11040089)
- Ledoux, P. 1947, *ApJ*, 105, 305, doi: [10.1086/144905](https://doi.org/10.1086/144905)
- Levesque, E. M., Massey, P., Olsen, K. A. G., et al. 2005, *ApJ*, 628, 973, doi: [10.1086/430901](https://doi.org/10.1086/430901)
- Lobel, A., & Dupree, A. K. 2000, *ApJ*, 545, 454, doi: [10.1086/317784](https://doi.org/10.1086/317784)
- . 2001, *ApJ*, 558, 815, doi: [10.1086/322284](https://doi.org/10.1086/322284)
- Maeder, A., & Meynet, G. 2000, *ARA&A*, 38, 143, doi: [10.1146/annurev.astro.38.1.143](https://doi.org/10.1146/annurev.astro.38.1.143)
- Mestel, L. 1968, *MNRAS*, 138, 359, doi: [10.1093/mnras/138.3.359](https://doi.org/10.1093/mnras/138.3.359)
- Michelson, A. A., & Pease, F. G. 1921, *ApJ*, 53, 249, doi: [10.1086/142603](https://doi.org/10.1086/142603)
- Montargès, M., Kervella, P., Perrin, G., et al. 2014, *A&A*, 572, A17, doi: [10.1051/0004-6361/201423538](https://doi.org/10.1051/0004-6361/201423538)
- Montargès, M., Norris, R., Chiavassa, A., et al. 2018, *A&A*, 614, A12, doi: [10.1051/0004-6361/201731471](https://doi.org/10.1051/0004-6361/201731471)
- Montargès, M., Kervella, P., Perrin, G., et al. 2016, *A&A*, 588, A130, doi: [10.1051/0004-6361/201527028](https://doi.org/10.1051/0004-6361/201527028)
- Montargès, M., Cannon, E., de Koter, A., et al. 2023, *A&A*, 671, A96, doi: [10.1051/0004-6361/202245398](https://doi.org/10.1051/0004-6361/202245398)
- Nhung, P. T., Hoai, D. T., Darriulat, P., et al. 2023, *RAA*, 23, 015004, doi: [10.1088/1674-4527/aca06f](https://doi.org/10.1088/1674-4527/aca06f)
- Nhung, P. T., Hoai, D. T., Tuan-Anh, P., et al. 2021, *MNRAS*, 504, 2687, doi: [10.1093/mnras/stab954](https://doi.org/10.1093/mnras/stab954)
- Norris, R. P., Baron, F. R., Monnier, J. D., et al. 2021, *ApJ*, 919, 124, doi: [10.3847/1538-4357/ac0c7e](https://doi.org/10.3847/1538-4357/ac0c7e)

- O’Gorman, E., Kervella, P., Harper, G. M., et al. 2017, *A&A*, 602, L10, doi: [10.1051/0004-6361/201731171](https://doi.org/10.1051/0004-6361/201731171)
- Ohnaka, K., Hofmann, K. H., Schertl, D., et al. 2013, *A&A*, 555, A24, doi: [10.1051/0004-6361/201321063](https://doi.org/10.1051/0004-6361/201321063)
- Ohnaka, K., Weigelt, G., & Hofmann, K. H. 2017, *Nature*, 548, 310, doi: [10.1038/nature23445](https://doi.org/10.1038/nature23445)
- Ohnaka, K., Weigelt, G., & Hofmann, K.-H. 2019, *ApJ*, 883, 89, doi: [10.3847/1538-4357/ab3d2a](https://doi.org/10.3847/1538-4357/ab3d2a)
- Ohnaka, K., Hofmann, K.-H., Benisty, M., et al. 2009, *A&A*, 503, 183, doi: [10.1051/0004-6361/200912247](https://doi.org/10.1051/0004-6361/200912247)
- Ohnaka, K., Weigelt, G., Millour, F., et al. 2011, *A&A*, 529, A163, doi: [10.1051/0004-6361/201016279](https://doi.org/10.1051/0004-6361/201016279)
- Paladini, C., Baron, F., Jorissen, A., et al. 2018, *Nature*, 553, 310, doi: [10.1038/nature25001](https://doi.org/10.1038/nature25001)
- Patton, R. A., Pinsonneault, M. H., Cao, L., et al. 2023, Spectroscopic identification of rapidly rotating red giant stars in APOKASC-3 and APOGEE DR16, doi: [10.48550/arXiv.2303.08151](https://doi.org/10.48550/arXiv.2303.08151)
- Paxton, B., Bildsten, L., Dotter, A., et al. 2011, *ApJS*, 192, 3, doi: [10.1088/0067-0049/192/1/3](https://doi.org/10.1088/0067-0049/192/1/3)
- Paxton, B., Cantiello, M., Arras, P., et al. 2013, *ApJS*, 208, 4, doi: [10.1088/0067-0049/208/1/4](https://doi.org/10.1088/0067-0049/208/1/4)
- Paxton, B., Marchant, P., Schwab, J., et al. 2015, *ApJS*, 220, 15, doi: [10.1088/0067-0049/220/1/15](https://doi.org/10.1088/0067-0049/220/1/15)
- Paxton, B., Schwab, J., Bauer, E. B., et al. 2018, *ApJS*, 234, 34, doi: [10.3847/1538-4365/aaa5a8](https://doi.org/10.3847/1538-4365/aaa5a8)
- Paxton, B., Smolec, R., Schwab, J., et al. 2019, *ApJS*, 243, 10, doi: [10.3847/1538-4365/ab2241](https://doi.org/10.3847/1538-4365/ab2241)
- Perryman, M. A. C., Lindegren, L., Kovalevsky, J., et al. 1997, *A&A*, 323, L49. <https://ui.adsabs.harvard.edu/abs/1997A&A...323L..49P>
- Privitera, G., Meynet, G., Eggenberger, P., et al. 2016a, *A&A*, 591, A45, doi: [10.1051/0004-6361/201528044](https://doi.org/10.1051/0004-6361/201528044)
- . 2016b, *A&A*, 593, A128, doi: [10.1051/0004-6361/201628758](https://doi.org/10.1051/0004-6361/201628758)
- Ramstedt, S., Mohamed, S., Vlemmings, W. H. T., et al. 2017, *A&A*, 605, A126, doi: [10.1051/0004-6361/201730934](https://doi.org/10.1051/0004-6361/201730934)
- Ramstedt, S., Vlemmings, W. H. T., Doan, L., et al. 2020, *A&A*, 640, A133, doi: [10.1051/0004-6361/201936874](https://doi.org/10.1051/0004-6361/201936874)
- Rui, N. Z., & Fuller, J. 2021, *MNRAS*, 508, 1618, doi: [10.1093/mnras/stab2528](https://doi.org/10.1093/mnras/stab2528)
- Sana, H., de Mink, S. E., de Koter, A., et al. 2012, *Science*, 337, 444, doi: [10.1126/science.1223344](https://doi.org/10.1126/science.1223344)
- Schwarzschild, M. 1975, *ApJ*, 195, 137, doi: [10.1086/153313](https://doi.org/10.1086/153313)
- Shiber, S., Chatzopoulos, E., Munson, B., & Frank, J. 2023, Betelgeuse as a Merger of a Massive Star with a Companion. <https://ui.adsabs.harvard.edu/abs/2023arXiv231014603S>
- Smith, N. 2014, *ARA&A*, 52, 487, doi: [10.1146/annurev-astro-081913-040025](https://doi.org/10.1146/annurev-astro-081913-040025)
- Spruit, H. C. 2002, *A&A*, 381, 923, doi: [10.1051/0004-6361:20011465](https://doi.org/10.1051/0004-6361:20011465)
- Stock, J. W., Kitzmann, D., & Patzer, A. B. C. 2022, *MNRAS*, 517, 4070, doi: [10.1093/mnras/stac2623](https://doi.org/10.1093/mnras/stac2623)
- Stock, J. W., Kitzmann, D., Patzer, A. B. C., & Sedlmayr, E. 2018, *MNRAS*, 479, 865, doi: [10.1093/mnras/sty1531](https://doi.org/10.1093/mnras/sty1531)
- Sullivan, J. M., Nance, S., & Wheeler, J. C. 2020, *ApJ*, 905, 128, doi: [10.3847/1538-4357/abc3c9](https://doi.org/10.3847/1538-4357/abc3c9)
- Tennyson, J., & Yurchenko, S. N. 2012, *MNRAS*, 425, 21, doi: [10.1111/j.1365-2966.2012.21440.x](https://doi.org/10.1111/j.1365-2966.2012.21440.x)
- Tennyson, J., Yurchenko, S. N., Al-Rafaie, A. F., et al. 2016, *JMoSp*, 327, 73, doi: [10.1016/j.jms.2016.05.002](https://doi.org/10.1016/j.jms.2016.05.002)
- Tremblay, P. E., Ludwig, H. G., Freytag, B., Steffen, M., & Caffau, E. 2013, *A&A*, 557, A7, doi: [10.1051/0004-6361/201321878](https://doi.org/10.1051/0004-6361/201321878)
- Uitenbroek, H., Dupree, A. K., & Gilliland, R. L. 1998, *AJ*, 116, 2501, doi: [10.1086/300596](https://doi.org/10.1086/300596)
- Van Leeuwen, F., ed. 2007, *Astrophysics and Space Science Library*, Vol. 350, *Hipparcos, the New Reduction of the Raw Data* (Dordrecht: Springer Netherlands), doi: [10.1007/978-1-4020-6342-8](https://doi.org/10.1007/978-1-4020-6342-8)
- Vink, J. S., de Koter, A., & Lamers, H. J. G. L. M. 2001, *A&A*, 369, 574, doi: [10.1051/0004-6361:20010127](https://doi.org/10.1051/0004-6361:20010127)
- Virtanen, P., Gommers, R., Oliphant, T. E., et al. 2020, *Nature Methods*, 17, 261, doi: [10.1038/s41592-019-0686-2](https://doi.org/10.1038/s41592-019-0686-2)
- Vlemmings, W. H. T., Khouri, T., De Beck, E., et al. 2018, *A&A*, 613, L4, doi: [10.1051/0004-6361/201832929](https://doi.org/10.1051/0004-6361/201832929)
- Wheeler, J. C., & Chatzopoulos, E. 2023, *Astronomy & Geophysics*, 64, 3.11, doi: [10.1093/astrogeo/atad020](https://doi.org/10.1093/astrogeo/atad020)
- Wheeler, J. C., Nance, S., Diaz, M., et al. 2017, *MNRAS*, 465, 2654, doi: [10.1093/mnras/stw2893](https://doi.org/10.1093/mnras/stw2893)
- Yoon, S.-C., & Cantiello, M. 2010, *ApJ*, 717, L62, doi: [10.1088/2041-8205/717/1/L62](https://doi.org/10.1088/2041-8205/717/1/L62)
- Young, J. S., Baldwin, J. E., Boysen, R. C., et al. 2000, *MNRAS*, 315, 635, doi: [10.1046/j.1365-8711.2000.03438.x](https://doi.org/10.1046/j.1365-8711.2000.03438.x)
- Yurchenko, S. N., Tennyson, J., Syme, A.-M., et al. 2022, *MNRAS*, 510, 903, doi: [10.1093/mnras/stab3267](https://doi.org/10.1093/mnras/stab3267)
- Zapartas, E., de Mink, S. E., Justham, S., et al. 2019, *A&A*, 631, A5, doi: [10.1051/0004-6361/201935854](https://doi.org/10.1051/0004-6361/201935854)